Electrochemical deposition of nanostructured manganese oxide on hierarchically porous graphene–carbon nanotube structure for ultrahigh-performance electrochemical capacitors

Shin-Ming Li [a,1], Yu-Sheng Wang [a,1], Shin-Yi Yang [a,1], Chia-Hong Liu [a], Kuo-Hsin Chang [a], Hsi-Wen Tien [a], Niann-Tsyr Wen [b], Chen-Chi M. Ma [a,**], Chi-Chang Hu [a,*]

[a] Department of Chemical Engineering, National Tsing Hua University, Hsin-Chu 30013, Taiwan
[b] Chung-Shan institute of Science and Technology, Armaments Bureau, M.N.D., Taoyuan, Taiwan

HIGHLIGHTS

► The a-MnO$_x$/GS–CNT is fabricated by combining the solution-assemble process and anodic deposition.
► The use of a-MnO$_x$ on the 3D GS–CNT material produces a specific capacitance of MnOx of 1200 F g^{-1}.
► The specific energy and specific power of a-MnO$_x$/GS–CNT are as high as 46.2 Wh kg^{-1} and 33.2 kW kg^{-1}.
► This work conceptually provides new chances for designing 3D graphene-based architecture.

GRAPHICAL ABSTRACT
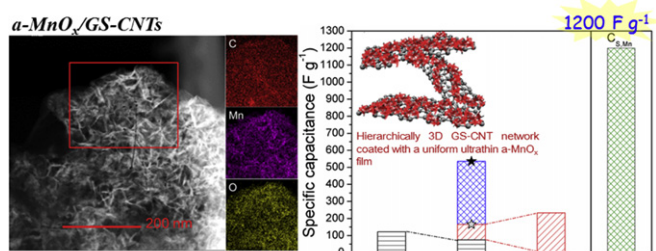
ABSTRACT

A 3D graphene sheet–carbon nanotube (GS–CNT) structure with a good wetting property, high porosity, and large surface area is homogeneously deposited with active amorphous manganese oxide (a-MnO$_x$) by potentiodynamic deposition. The flowery a-MnO$_x$ nanostructure with ultra-slender petals (ca. 5–8 nm) on the framework of hierarchically porous GS–CNT matrix not only enables nearly full utilization of a-MnO$_x$ but also retains sufficient conductivity and porosity for the high-rate charge–discharge application. The use of a-MnO$_x$ on the 3D GS–CNT material produces a specific capacitance of MnO$_x$ of 1200 F g^{-1} which is much-higher than that of a pure a-MnO$_x$ electrode ($C_{S,Mn}$ = 233 F g^{-1}). The specific energy and specific power of a-MnO$_x$/GS–CNT are respectively as high as 46.2 Wh kg^{-1} and 33.2 kW kg^{-1}, revealing that our work conceptually provides a way to produce porous structures composed of graphene, carbon nanotubes, and various electroactive materials for high-performance energy storage devices.

© 2012 Elsevier B.V. All rights reserved.

1. Introduction

With a rapid increase of the global energy consumption coupled with the severe climate change, settling the following two issues is very urgent and indispensable for scientists and engineers worldwide. The first issue is to develop the sustainable, renewable, and alternative energy sources with low emission of global-warming gases. Another crucial issue is the development of advanced

energy-storage systems to efficiently utilize the electricity generated from the intermittently renewable sources, such as solar and wind-power energies. Currently, electrochemical capacitors (ECs) have been considered as one of the most important energy-storage systems [1,2]. ECs, also called supercapacitors or ultracapacitors, have been proposed as an attractive energy-storage device due to their high-impact characteristics, including superior cycle life, high power ability, short charging time, and excellent reliability in comparing with batteries [1,2]. Based on the above advantages, ECs have been combined with batteries or fuel cells to fabricate an advanced power system for various applications, such as portable systems, hybrid electric vehicles, electric vehicles, and large-scale power and energy management [3].

From previous investigations, porous carbon-based materials, conducting polymers, and transition metal oxides are potential candidates for the electrode materials of ECs [3,4]. They generally involve two types of energy storage mechanisms, i.e., capacitance from the electrical double layer charge/discharge and pseudo-capacitance from the superficial redox couples [3,4]. Among these electrode materials, transition metal oxides have drawn a great and extensive research attention due to their large specific capacitance, resulted from fast and reversible redox reactions at the surface of active materials. Nowadays, many efforts on ECs aim at exploring alternative metal oxides to replace RuO_2 in commercial pseudo-capacitors because of high cost and rareness of Ru [4,5]. Among the proposed metal oxides, manganese oxides (MnO_x) have been widely investigated due to the low cost, environmental benignity, and ultrahigh theoretical specific capacitance ($C_{S,Mn} \sim 1370$ F g^{-1}) [6]. Unlike RuO_2, MnO_x was operated in neutral aqueous electrolytes, which provide a further advantage for the commercial application. However, the poor electrical conductivity is the main drawback of MnO_x; as a result, its performance is usually much lower than the theoretical value estimated from its redox reaction [4,7]. Accordingly, many efforts have been paid for promoting the capacitive performances of MnO_x. Due to the high power requirement, the pseudo-capacitive redox reactions generally involve MnO_x in the very thin surface layer and the ideal performances of pure MnO_x were only observed under the extreme case with very low mass loadings, limiting the practical applicability. To date, incorporation of nanostructured MnO_x into a porous conductive substrate is the most promising approach to simultaneously keep smooth pathways of electrons and ions for the pseudo-capacitive redox transitions to promote the utilization of MnO_x [2,8,9]. Thus, a significant enhancement in capacitive performances of many MnO_x/carbon composites (see Table 1) has been demonstrated [8–14]. Based on these examples, the key in developing MnO_x/carbon composites with excellent capacitive performances is to fabricate a conformal coating of ultrathin MnO_x onto a porous, conductive

substrate with high specific surface area to optimize the microstructure of hybrid materials and to fully utilize MnO_x.

Recently, graphene sheet (GS) is regarded as a next-generation electrode material for energy storage and conversion systems due to its unique properties, such as ultrahigh theoretical surface area (2630 m^2 g^{-1}), sufficient porosity, superior conductivity, and rich surface chemistry [15,16]. Accordingly, intensive efforts have been paid to use various technologies to synthesize MnO_x/GS composites for the electrode materials of ECs [5,10,12,14]. However, the aggregated issue will ruin the advantage of ultrahigh theoretical surface area of GS due to the fact that the physicochemical properties of aggregated GS are similar to graphite [17,18]. Hence, the actual performances of graphene-based materials are usually lower than the anticipative value estimated from the theoretical surface area. Therefore, how to effectively improve the performances of graphene-based materials is a crucial issue to explore its potential to the energy storage/conversion applications.

In this work, a hierarchically porous structure, consisting of nano-structured a-MnO_x, 2D GS and 1D carbon nanotubes (CNTs), is designed to approach the full utilization of electroactive materials (i.e., a-MnO_x) meanwhile this idea is also suitable for other electroactive materials. Note that CNTs in the hybrid mainly act as a spacer avoiding the restacking of graphene because the specific surface area of CNTs is low. Consequently, 10 wt% CNTs is a compromise content for obtaining the maximal specific surface area of this series of hybrids [17]. As shown in Fig. 1, a two-step approach is developed to fabricate the 3D a-MnO_x/GS−CNT composite with hierarchical porosity. The first step is to insert 1D CNTs into the layers of chemically functionalized GS to construct a mesoporous GS−CNT structure via a simple solution-assemble process [17]. In the second step, a-MnO_x is grown as flowery nanostructures with ultra-slender petals (about 5−8 nm) along the framework of a porous GS−CNT matrix via potentiodynamic deposition. This 3D porous network coated with a uniform ultra-thin a-MnO_x film is characterized for the supercapacitor application. Clearly, this work develops a simple, efficient and practical approach to fabricate a novel porous manganese oxide/graphene-based composite electrode with outstanding capacitive performances through combining the simple solution-assemble process and the reproducible electrochemical deposition technology. Moreover, the total specific capacitance of a-MnO_x/GS−CNTs is higher than those previously reported in the literature on the basis of MnO_x/graphene electrode materials (see Table 1) [10,12–14,19]. Most importantly, this work conceptually provides a way in designing a 3D porous graphene-based matrix for many electroactive materials.

2. Experimental

2.1. Synthesis of graphene oxide (GO)

The preparation of GO completely follows the modified Hummer's method [20]. 0.25 g graphite and 0.125 g $NaNO_3$ were added into a 100-ml flask filled with 12 ml H_2SO_4 (98%) in an ice bath under stirring. Next, 0.75 g $KMnO_4$ was added slowly to the solution, keeping the temperature below 15 °C. Then, the ice bath was removed and the flask was heated to 50 °C, followed by a slow addition of 12 ml deionized (DI) water. The temperature of the solution was increased to 98 °C and the solution was maintained at this temperature for 15 min. Next, 50 ml DI water with 10% H_2O_2 was added to the solution until the cessation of gas evolution. The solution was centrifuged at 11,000 rpm and washed with DI water for several times to remove the impurities. Finally, the solution was dried at 40 °C in a vacuum oven for three days to obtain GO powders.

Table 1
Performances of a-MnO_x/carbon hybrid electrodes for ECs.

Method[a]	Description[b]	Electrolyte	$C_{S,T}$ F g^{-1} (scan/discharge rate)	Reference (year)
RD	nr-Mn_3O_4/GS	Na_2SO_4	121 (0.5 A g^{-1})	14 (2012)
ED	GS/nw-MnO_2-textile	Na_2SO_4	315 (2 mV s^{-1})	19 (2011)
RD	ns-MnO_2/GS	Na_2SO_4	188 (0.25 A g^{-1})	12 (2011)
MI	np-MnO_2/GS	Na_2SO_4	303 (10 mV s^{-1})	11 (2011)
MI	np-MnO_2/GS	Na_2SO_4	310 (2 mV s^{-1})	13 (2011)
RD	nr-MnO_2/GO	Na_2SO_4	197.2 (0.2 A g^{-1})	10 (2010)
RD	np-MnO_x/CNT	K_2SO_4	290 (10 mV s^{-1})	9 (2010)
ED	nf-MnO_x/GS−CNT	Na_2SO_4	535 (5 mV s^{-1})	This work

[a] RD = redox deposition, ED = electrodeposition, MI = microwave irradiation.
[b] nw = nanowire, nf = nanoflower, np = nanoparticle, nr = nanorod, ns = nanosheet, GS = graphene nanosheet, GO = graphene oxide, MC = mesoporous carbon, CNT = carbon nanotube.
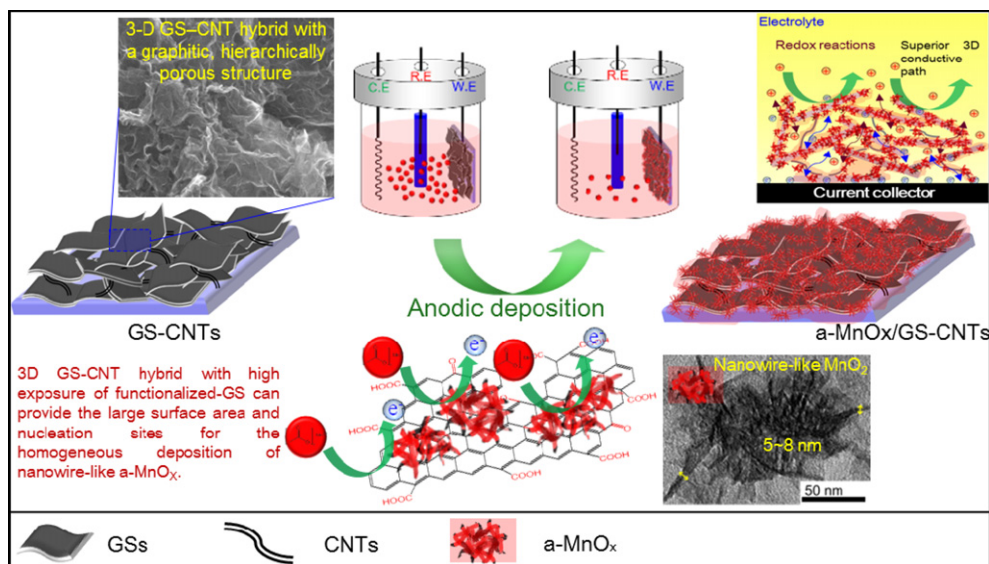
Fig. 1. Illustration of the procedure for fabricating the 3D mesoporous a-MnO$_x$/GS−CNT composite.

2.2. Preparation of GS−CNT hybrids

The preparation procedure of chemically functionalized GS−CNT hybrids mainly follows our previous work [17]. The raw multiwalled carbon nanotubes (MWCNTs) with an average diameter equal to 20 nm are commercially available (model: Ctube 100, CNT Co., Ltd., Incheon, Korea). In order to purify the MWCNTs, 250 mg MWCNTs were added into a 500-ml flask filled with an aqueous solution of 30 wt% HCl. The solution was maintained at room temperature under magnetic stirring for 2 h and then, the MWCNTs were obtained by centrifuging at 11,000 rpm and washed with DI water for several times to remove impurities. The solution was dried at 40 °C under vacuum for three days to obtain purified MWCNTs. For preparing GS−CNT hybrids, the GO/MWCNT in a weight ratio of 9/1 was first added into a DI water solution with ethylene glycol (EG) in an ice bath under ultrasonication for 2 h. Next, the solution was heated to 90 °C with magnetic stirring for 24 h and separated by filtration through a polytetrafluoroethylene (PTFE) membrane with the pore size of 0.25 μm. The filtered powders were washed several times with DI water and further dispersed in an ultrasonic ethanol bath for 2 h to form well-dispersed inks. The ink was dropped onto the surface of pre-polished graphite substrates to prepare the GS−CNT electrode. The pre-polished graphite substrates were prepared completely according to our previous work [21]. The exposed geometric area of these pre-treated graphite supports is 1 cm^2 while the other surface areas were insulated with PTFE coatings. The mass loading of GS−CNT hybrid is carefully controlled to be ca. 0.5 mg cm^{-2}.

2.3. Electrochemical deposition of a-MnO$_x$

For a pure a-MnO$_x$ electrode, MnO$_x$ was potentiodynamically deposited onto the pretreated graphite substrate through cyclic voltammetry (CV) at 25 mV s^{-1} between 0.1 and 1.0 V for 20 cycles according to our previous work [19]. For preparing a-MnO$_x$/GS and a-MnO$_x$/GS−CNT electrodes, the procedure is similar to that of the pure a-MnO$_x$ electrode while the pretreated graphite substrate were coated with GS and GS−CNT before the potentiodynamic deposition. After deposition, the electrodes were rinsed with DI

water and dried in a vacuum oven at room temperature overnight. The average mass loading of a-MnO$_x$ on the pure a-MnO$_x$ and a-MnO$_x$/GS−CNT electrodes, equal to 0.25 ± 0.01 mg cm^{-2}, was carefully controlled by the number of CV cycles, which was determined by a microbalance with an accuracy of 10 μg more than 6 times. The standard deviation of this mass measurement is less than 4%.

2.4. Material characterization and instruments

The topography of GS−CNT hybrids was identified by an atomic force microscope (AFM, Digital Instrument D3100). X-ray photoelectron spectra (XPS) were measured using a VG Scientific ESCALAB 220 iXL spectrometer with an Al Kα ($hv = 1486.69$ eV) X-ray source. Transmission electron microscopic (TEM) analyses were conducted on a Philips Tecnai F20 G2 electron microscope at 200 kV. Samples for TEM examinations were prepared by drop casting on Cu grids followed by solvent evaporation in air at room temperature. The surface morphologies of a-MnO$_x$ and a-MnO$_x$/GS−CNTs were investigated by a field emission-scanning electron microscope (FE-SEM, Hitachi S-4700 I, Japan).

2.5. Electrochemical characterization

CV was conducted by an electrochemical analyzer system, CHI 633A (CH Instruments, USA). The electrochemical impedance spectrum (EIS) analyzer, IM6 with Thales software (ZAHNER, Germany), was employed to measure and analyze the EIS spectra. The potential amplitude of ac was equal to 10 mV meanwhile the frequency range was from 10 kHz to 100 mHz. All the electrochemical analysis was carried out in a three-compartment cell. An Ag/AgCl (Argenthal, 207 mV vs. standard hydrogen electrode at 25 °C) was used as the reference electrode, and a platinum wire with an exposed area equal to 4 cm^2 was employed as the counter electrode. A Luggin capillary, whose tip was set at a distance of 2 mm from the surface of the working electrode, was used to minimize errors due to the IR drop in the electrolytes. All solutions used in this work were prepared with 18 MΩ cm DI water produced by a reagent water system (MILLI-Q SP, Japan), and all reagents not otherwise specified in this work were Merck, GR.

3. Results and discussion

3.1. Morphology and microstructure of a-MnO$_x$/GS–CNT composites

Fig. 2 shows the typical morphologies and microstructures of GS–CNT, pure a-MnO$_x$, and a-MnO$_x$/GS–CNT, examined through the FE-SEM images. Based on our previous study [17], the morphology and microstructure of GS showed the coplanar alignment of 2D graphene into layered aggregates due to the strong van der Waals interactions among GS. The layer-stacked GS shows relatively smooth, compact and planar morphology [17]. In comparing with GS, the morphology of the 3D GS–CNT nano-network shows a highly porous, crumpled, and loose structure, revealing that CNTs have been successfully inserted into the GS layers to effectively inhibit the restacking of GS via the simple solution-assemble process [17]. Therefore, this 3D GS–CNT nano-network is proposed to be an advanced platform for coating thin-layer electroactive materials. The SEM image of pure a-MnO$_x$ in Fig. 2(c) shows that large a-MnO$_x$ grains significantly stack and aggregate together. Although the large oxide grains are composed

of a-MnO$_x$ wire-like nanosheets (ca. 10–15 nm in Fig. 2(d)), the thick, compact, and dense structure generally limits the diffusion of electrolyte and cations toward the interface of all entangled oxide nanowires/sheets, resulting in the low utilization of a-MnO$_x$. In comparison with pure a-MnO$_x$, a-MnO$_x$/GS–CNT shows a much more crumpled, rougher and looser structure (see Fig. 2(e)). a-MnO$_x$ was found to uniformly grow onto the framework of 3D porous GS–CNT matrix in the form of flowery nanostructures with ultrathin petals (ca. 5–8 nm in Fig. 2(f)). This result reveals that the porous GS–CNT matrix acts as an ideal platform for a-MnO$_x$ deposition due to the highly porous and unique 3D graphene-based conductive network.

In order to further realize and investigate the microstructure of a-MnO$_x$ grown on the GS–CNT matrix, scanning transmission electron microscopic (STEM) element mapping is employed to observe the distribution of a-MnO$_x$ on the surface of GS–CNT. A dark field TEM image and the corresponding element mapping images of carbon, manganese and oxygen are shown in Fig. 3. The uniform distribution of manganese and oxygen elements along with carbon over the whole area of a-MnO$_x$/GS–CNT confirms the
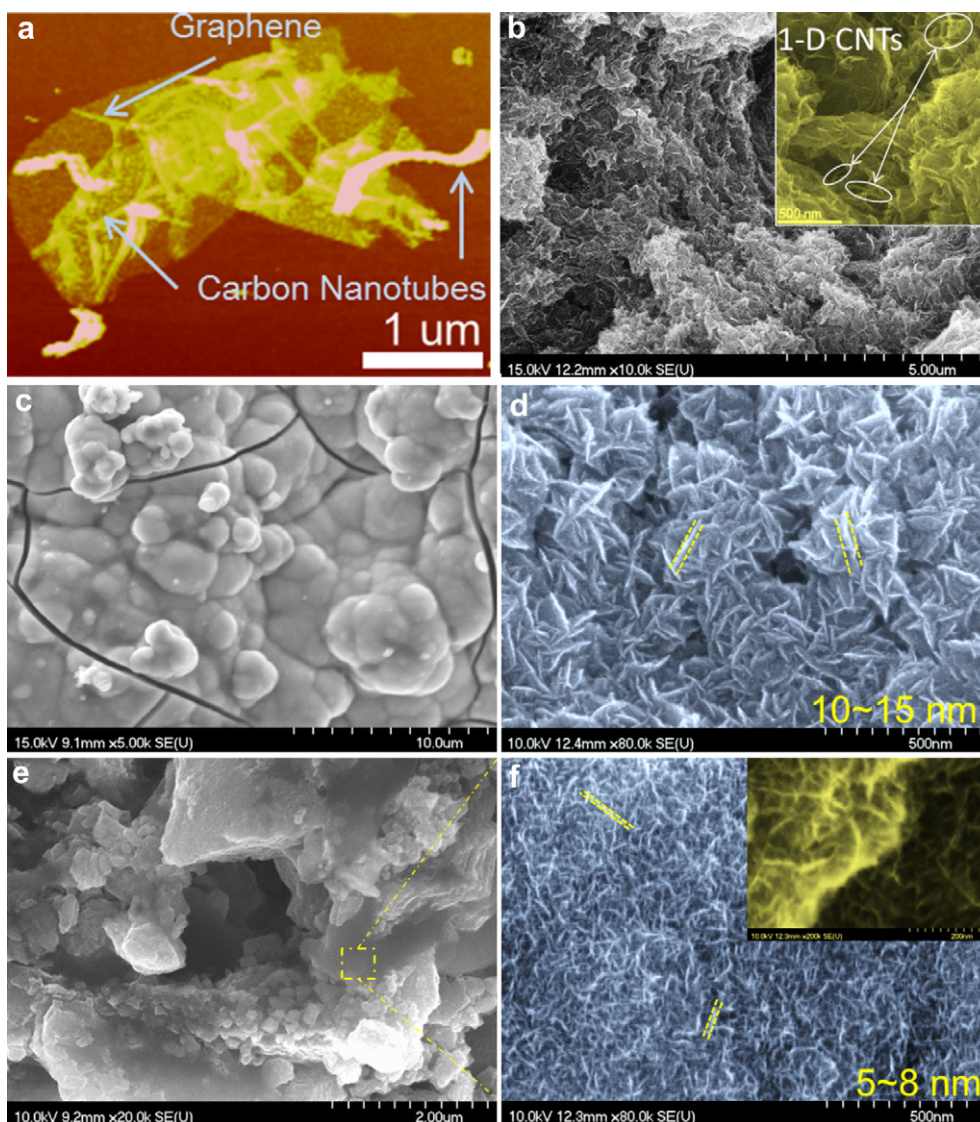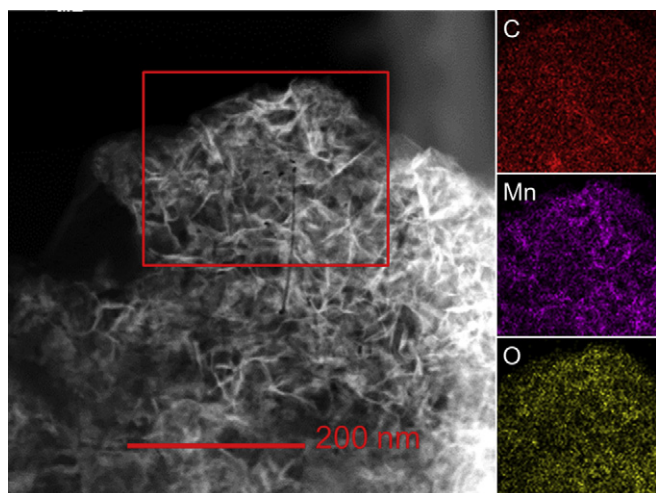

Fig. 2. (a) AFM and (b) SEM images of a GS–CNT hybrid, inset in (b) is the SEM image with high magnification. SEM images of (c, e) low and (d, f) high magnifications for (c, d) a-MnO$_x$ and (e, f) a-MnO$_x$/GS–CNT, inset in (f) is the SEM image with the magnification of 200 K.

Fig. 3. STEM element mapping analyses of carbon, oxygen and manganese of a-MnO$_x$/GS–CNTs composite electrode.

homogeneous growth of a-MnO$_x$ nano-petals on the whole surface of the GS–CNT framework. Based on our previous research [17], the 3D hierarchically porous GS–CNT structures not only provide large surface area and high porosity to generate superior electrical double layer capacitance but also possess residual oxygen functionalities on the EG-reduced GS surface to enable large pseudo-capacitance. The good wetting property, high porosity, and large surface area of the electrolyte-accessible GS–CNT framework is expected to facilitate the diffusion of Mn precursor into the interior region of GS–CNT. Hence, a homogeneous a-MnO$_x$ thin-film consisting of slender oxide nanowires/sheets is successfully deposited

on the surface of GS–CNT framework in comparing with the electrode consisting of thick, compact, and dense pure a-MnO$_x$. Based on the above comparison and findings, the pathways of both electron and electrolyte within this novel hierarchical a-MnO$_x$/GS–CNT matrix must be promoted. This will lead ultrahigh utilization of a-MnO$_x$, especially due to the significant improvement in the electronic conductivity of MnO$_x$-based materials.

3.2. Comparisons of the capacitive behavior of all electrodes

To explore the advantages of a-MnO$_x$/GS–CNT composites as the EC electrode material, the capacitive properties of the composite electrodes were investigated by means of CV and EIS measurements. In Fig. 4(a), CV curves of GS–CNT, a-MnO$_x$, and a-MnO$_x$/GS–CNT electrodes measured at 5 mV s^{-1} show nearly rectangular curves, demonstrating their ideal properties for the ECs application. The response current density of a-MnO$_x$/GS–CNT is much higher than that of pure a-MnO$_x$, indicating that a-MnO$_x$/GS–CNT possesses much better electrical conductivity and higher utilization of active Mn species. Fig. 4(b)–(d) show the CV curves of all electrodes with the scan rate varying from 5 to 200 mV s^{-1}. Due to the physical charge/discharge mechanism of the electrical double layer, the GS–CNT electrode generally exhibits a much-better rate capability even when the scan rate is as high as 200 mV s^{-1} (Fig. 4(b)) while an askew CV behavior is observed for the pure a-MnO$_x$ electrode at high scan rates (Fig. 4(c)). This is reasonably due to the poor conductivity of a-MnO$_x$ [22]. Unlike the poor CV responses of pure a-MnO$_x$, the CV curve of a-MnO$_x$/GS–CNT still displays more capacitive-like responses at 200 mV s^{-1}, implying that the GS–CNT backbone of the composite enhances the porosity and electronic conductivity of a-MnO$_x$/GS–CNT to simultaneously facilitate the ion and electron transport during the high-rate charge and discharge processes.
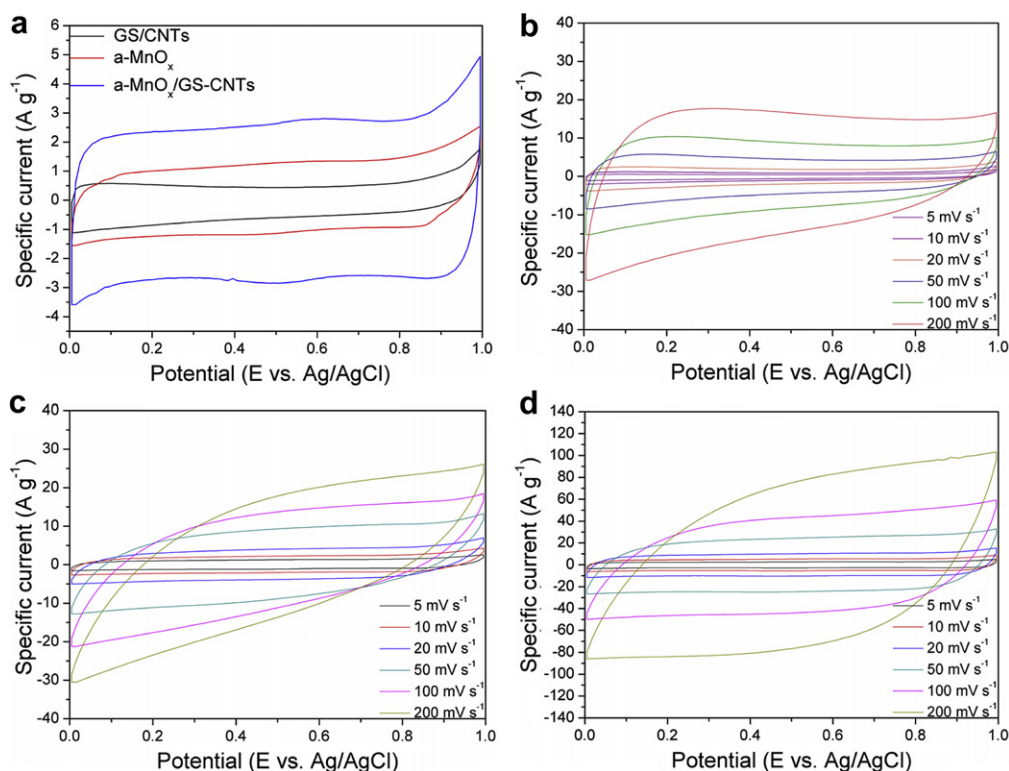
Fig. 4. (a) CV curves measured at 5 mV s^{-1} for GS–CNT, a-MnO$_x$ and a-MnO$_x$/GS–CNT electrodes. CV curves of (b) GS–CNT, (c) a-MnO$_x$ and (d) a-MnO$_x$/GS–CNT measured at various scan rates in 0.5 M Na$_2$SO$_4$.

Fig. 5 shows the total specific capacitance ($C_{S,T}$) of all electrode materials and the specific capacitance of a-MnO_x ($C_{S,Mn}$ in the 4th column) dispersed in a-MnO_x/GS−CNT. The total specific capacitance was estimated from the CV curves of GS−CNT, pure a-MnO_x and a-MnO_x/GS−CNT shown in Fig. 4 according to equation (1):

$$C_{S,T} = \frac{\int i dV}{\nu W \Delta V} \tag{1}$$

where i is the response current density (A cm^{-2}), ΔV is the potential window (V), ν is the potential scan rate (V s^{-1}) and W is the total weight of electrode materials (g cm^{-2}).

Clearly, $C_{S,T}$ of a-MnO_x/GS−CNT (ca. 535 F g^{-1}) is much higher than that of pure a-MnO_x (233 F g^{-1}) and GS−CNT (ca. 140 F g^{-1}), which is also much higher than those of MnO_x/graphene electrode materials reported previously [10,12,13,19,23]. The area-normalized capacitances ($C_{S,A}$) can be further calculated on the basis of the geometric area of the graphite substrates (1 cm^2). The $C_{S,A}$ value of a-MnO_x/GS−CNT (4.01×10^5 μF cm^{-2}) is also much higher than that of pure a-MnO_x (5.8×10^4 μF cm^{-2}) and GS−CNT (7×10^4 μF cm^{-2}), which is consistent with the result of $C_{S,T}$. Consequently, the above phenomenon is believed to result from the good electron transport pathways provided by the GS−CNT framework and the electrolyte penetration property within the whole matrix of a-MnO_x/GS−CNT. Note that the gray and red areas in the 2nd column respectively indicate the theoretical capacitance contributed from GS−CNT and a-MnO_x according to their weight factions. Here the theoretical capacitance, $C_{S,T,theo}$, is estimated from the weight fraction of pure a-MnO_x and GS−CNT in the a-MnO_x/GS−CNT electrode according to equation (2):

$$C_{S,T,theo} = C_{S,C} \times W_C + C_{S,p-Mn} \times W_{Mn} \tag{2}$$

where $C_{S,C}$ and $C_{S,p-MN}$ represent the specific capacitance of GS−CNT electrode and pure a-MnO_x electrode, respectively. W_C and W_{Mn} indicate the weight fraction of GS−CNT and a-MnO_x within the a-MnO_x/GS−CNT electrode. The blue area, an enhanced capacitance, results from a synergistic effect (in utilizing a-MnO_x and the double-layer capacitance) between a-MnO_x and GS−CNT.

In order to gain a further understanding about the utilization of active materials within a-MnO_x/GS−CNT, $C_{S,Mn}$ is deduced after

subtracting the contribution from GS−CNT according to equation (3) [21], revealing an ultrahigh value ($\sim$1200 F g^{-1}).

$$C_{S,Mn} = \frac{C_{S,T} - (1 - W_{Mn})C_{S,C}}{W_{Mn}} \tag{3}$$

In comparison with pure a-MnO_x, introducing GS−CNT as the conductive backbone yields a great improvement in the utilization of a-MnO_x (ca. 5 times increase in the specific capacitance). Such ultrahigh capacitance, very close to the theoretical specific capacitance of MnO_x (i.e., $C_{S,Mn,theo} \sim 1370$ F g^{-1}), reveals the nearly full utilization of electroactive materials within a-MnO_x/GS−CNT [8,9]. This outstanding performance is mainly attributed to the even dispersion of a-MnO_x nanostructure with slender oxide nanowires/sheets over the 3D porous GS−CNT structure. This property not only improves the electronic conductivity of electrode materials but also facilitates the ion transport in and out of the homogeneous oxide layer in order to provide much more electrolyte-accessible sites for the intercalation of Na$^+$ and H$^+$ [6].

To further emphasize the excellent capacitive performances of a-MnO_x/GS−CNT, the power capability of all electrode materials investigated in this work was compared by changing the scan rate of CV. Fig. 6(a) and (b) shows the dependence of the capacitive current density and $C_{S,T}$ of GS−CNT, pure a-MnO_x and a-MnO_x/GS−CNT on the scan rate of CV. In Fig. 6(a), two slopes are

Fig. 5. The total specific capacitance ($C_{S,T}$) of all electrode materials (left section), and the utilization of a-MnO_x ($C_{S,Mn}$) for the a-MnO_x/GS−CNT composite (right section). The theoretical value is estimated from the weight fractions of a-MnO_x and GS−CNT in the composite.
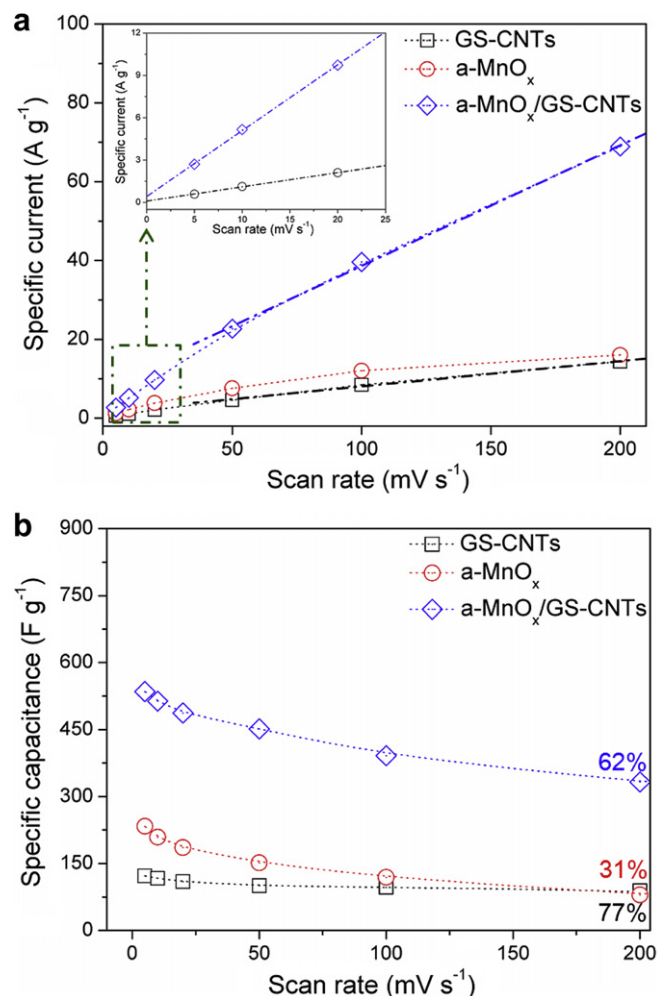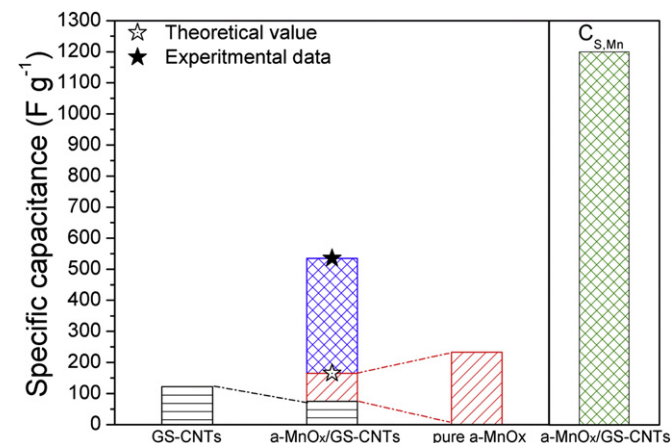

Fig. 6. Dependence of (a) current density and (b) total specific capacitance ($C_{S,T}$) of GS−CNT, a-MnO_x and a-MnO_x/GS−CNT on the CV scan rate from 5 to 200 mV s^{-1}. Inset in (a) is the magnified portion near the origin, illustrating the high power-capability for GS−CNT and a-MnO_x/GS−CNT.

clearly found for the dependence of the capacitive current density of a-MnO$_x$/GS−CNT and GS−CNT on the scan rate of CV varied from 5 to 200 mV s^{-1}. The above two slopes for the GS−CNT hybrid is attributable to the relatively slow redox kinetics of residual oxygen-containing functional groups on GS−CNT, which is consistent to the results in previous reports [24,25]. The oxygen-containing functional groups on the surface of carbon-based materials would provide the pseudo-capacitance, resulting in a change in slop with increasing the scan rate in the slow scan-rate region [24,25]. Similarly, due to the relatively slow electrochemical kinetics of the superficial redox couples, the pseudo-capacitive contribution from electroactive manganese oxide on pure a-MnO$_x$ and a-MnO$_x$/GS−CNT will decrease with increasing the scan rate of CV. On the other hand, both electrode materials show the high-power capability from the quasi-linear dependence of capacitive current density on the scan rate of CV in the high scan-rate region. This result reveals that GS−CNT can provide the smooth pathways for electron conduction and electrolyte diffusion within the a-MnO$_x$/GS−CNT composite to reduce the equivalent series resistance (ESR). From Fig. 6(b), only about 38% capacitance loss is found when the scan rate is increased from 5 to 200 mV s^{-1}. This good retention in the total specific capacitance for a-MnO$_x$/GS−CNT is much better than that for pure a-MnO$_x$ (ca. 70% loss), which is a great benefit to the EC application. Based on all the above results and discussion, a-MnO$_x$/GS−CNT exhibits much higher energy and power densities as well as capacitance retention in comparison with a-MnO$_x$ although the capacitance retention of GS−CNT is superior among these three electrode materials (ca. 29% loss). All these unique capacitive properties reasonably result from the highly porous, 3D, hierarchical structure of a-MnO$_x$/GS−CNT.

3.3. Enhanced capacitive responses of a-MnO$_x$/GS−CNT

To further emphasize the excellent capacitive performances of a-MnO$_x$/GS−CNT, the electrochemical impedance spectroscopic (EIS) responses of the above three materials are investigated and Fig. 7 shows the typical negative Nyquist spectra measured at 0.5 V in 0.5 M Na$_2$SO$_4$. From a comparison of all EIS responses, several features are worthy being mentioned. First, all EIS spectra in the low frequency end show capacitive-like behavior although the phase angle indicates certain deviations from the ideal capacitor behavior. Moreover, the order of materials with respect to increasing the phase angle deviation is: GS−CNT (6.7°) < a-MnO$_x$/GS−CNT (15.5°) < a-MnO$_x$ (27.2°). Thus, the capacitive behavior of a-MnO$_x$ has been improved by introducing the GS−CNT framework. Second, all spectra show a depressed semicircle from the high-frequency end to the middle-frequency region (see the inset of Fig. 7), revealing the porous electrode nature. The small and unclear impedance arcs on spectra 1 and 3 indicate a near planar electrode behavior [21], attributable to the highly porous microstructures of GS−CNT and a-MnO$_x$/GS−CNT. For pure a-MnO$_x$, the impedance arc is large and obvious, indicative of the largest charge transfer resistance (ca. 0.7 Ω), reasonably attributed to its poor electronic conductivity and relatively compact nature. As a result, the charge transfer resistance of both electrodes is much smaller than that of a-MnO$_x$. This phenomenon is attributable to the following two reasons. (1) Beside the good electronic conductivity of GS, the 1-D CNTs also bridge the gaps between GS to form the electron-conductive network to effectively reduce the impedance of electrode materials. (2) The ultrathin a-MnO$_x$ nanowires/sheets embedded on the highly conductive GS−CNT framework result in a low charge transfer resistance of electroactive materials. Third, the 45° slope of the Warburg diffusion behavior in the middle-frequency region for pure a-MnO$_x$ (see spectra 2 in inset of Fig. 7) implies that the relatively compact structure limits the diffusion of ions into the interior of a-MnO$_x$ agglomerates. In contrast, the Warburg diffusion behavior in the middle-frequency region is not visible for both GS−CNT and a-MnO$_x$/GS−CNT electrodes, revealing that the 3D porosity within the GS−CNT network exhibits enhanced electrolyte diffusion and charge-transfer rates. This result implies that superficial redox couples of the a-MnO$_x$ nanostructure with ultrathin nano-petals (ca. 5−8 nm) on the GS−CNT matrix retain sufficient high electrochemical reversibility for high-rate charge storage and delivery. Therefore, a-MnO$_x$/GS−CNT possesses excellent performances for the ECs application.

3.4. Superior capacitive performances of a-MnO$_x$/GS−CNT

The plot of specific power (SP) against specific energy (SE) is a very important index for the electrode materials of ECs, where the average values of SE and SP can be calculated on the basis of equations (4) and (5) [26]:

$$SE = \frac{C_{S,T}(\Delta V)^2}{2} \times \frac{1000}{3600} \qquad (4)$$

$$SP = \frac{SE}{t} \times 3600 \qquad (5)$$

where SE indicates the average specific energy (Wh kg^{-1}), $C_{S,T}$ is the total specific capacitance (F g^{-1}) of electrode materials, ΔV is the working potential window (V), SP is the average specific power (W kg^{-1}), and t, in general, is the discharge time (s). For a relatively long current drain time (200 sec) shown in Fig. 8, the specific energy and specific power of a-MnO$_x$/GS−CNT is equal to 74.3 Wh kg^{-1} and 1338 W kg^{-1}, respectively, which are much higher than those of GS−CNT and pure a-MnO$_x$. Furthermore, the specific energy of a-MnO$_x$/GS−CNT is still as high as 46.2 Wh kg^{-1} when the specific power reaches 33.248 kW kg^{-1}, revealing the superior performances of this 3D hierarchical a-MnO$_x$/GS−CNT composite for the next generation ECs.

To further evaluate the EC performance, the cycle stability of a-MnO$_x$/GS−CNTs under repeated charge and discharge cycles
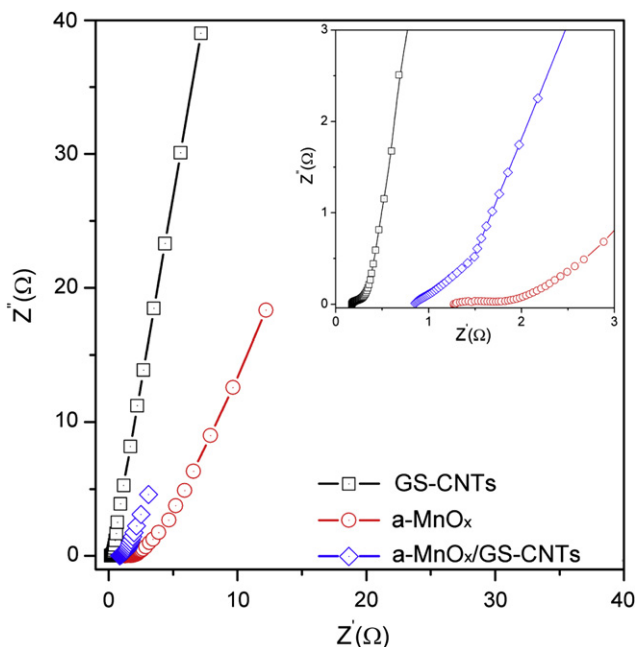

Fig. 7. EIS spectra of GS−CNT, a-MnO$_x$ and a-MnO$_x$/GS−CNT measured at 0.5 V in 0.5 M Na$_2$SO$_4$. The inset is a magnified portion of the plot near the origin.
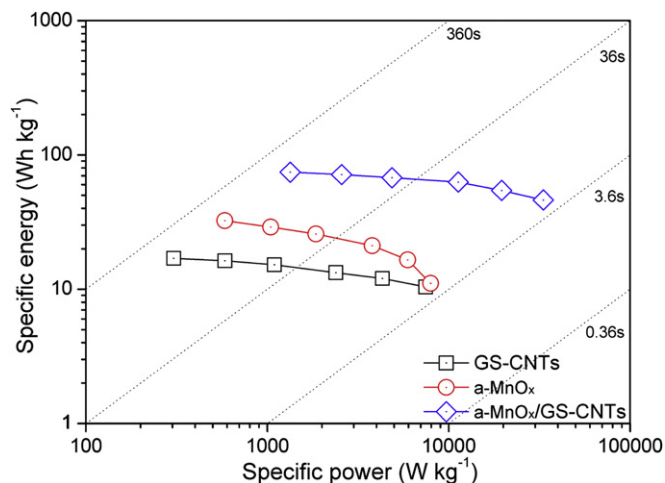
Fig. 8. The specific energy vs. specific power plot for GS–CNT, a-MnO$_x$ and a-MnO$_x$/GS–CNT electrodes.

between 0 and 1 V at 50 mV s^{-1} is shown in Fig. 9. The result demonstrates that a-MnO$_x$/GS–CNTs exhibits excellent cycling stability, where the capacitive loss after 1500 cycles is only 1.42%. Based on previous reports [27,28], the cycle stability of a-MnO$_x$ can
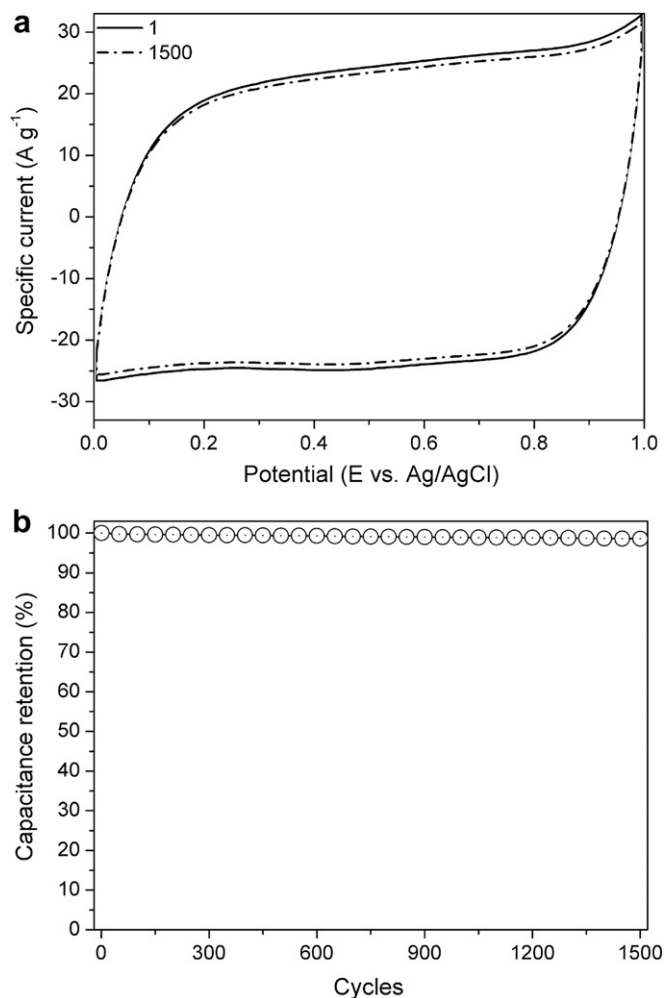

Fig. 9. (a) Cyclic voltammograms against cycle number and (b) capacitance retention against cycle number for a-MnO$_x$/GS–CNT in the 0.5 M Na$_2$SO$_4$. A scan rate of 50 mV s^{-1} was used.

be further improved through adding small amounts of NaHCO$_3$ or Na$_2$HPO$_4$ into neutral aqueous electrolytes since the oxide disso-lution and gas evolution phenomena were successfully suppressed by the formation of insoluble Mn(HCO$_3$)$_{4-2y}$(CO$_3$)$_y$ or the adsorp-tion of HPO$_4{}^{2-}$. We believe that the above concept in adding small amounts of NaHCO$_3$ or Na$_2$HPO$_4$ is applicable to the a-MnO$_x$-based electrode for further enhancing the cycle stability, showing its promising application potential for ECs.

According to the above electrochemical illustrations, a-MnO$_x$/GS–CNT exhibits the best capacitive performances in comparison with GS–CNT and pure a-MnO$_x$. The remarkable results of this composite are attributable the following reasons. (i) The CNTs function as a conductive nanospacer which effectively reduces the restacking of GS and greatly enhances the exposure of GS to form the porous GS–CNT structure with large electrolyte-accessible surface area, high porosity, and a 3D conductive framework. (ii) The 3D GS–CNT material with a good wetting property, high porosity and large electrolyte-accessible surface area can serve as an ideal and prom-ising platform for depositing electroactive species, leading to the homogeneous coating of ultrathin a-MnO$_x$ nanowires/sheets. (iii) The ultrathin a-MnO$_x$ film embedded on the highly conductive GS–CNT framework possesses an excellent interfacial contact between a-MnO$_x$ and GS–CNT, resulting in the acceleration of electron transport within the ternary composite. (iv) a-MnO$_x$ grown on GS–CNT exhibits a unique nanostructure with ultrathin nano-petals (ca. 5–8 nm), which not only enables a much larger electrochemically active surface area for the reversible pseudo-capacitive reactions but also remains a sufficient porosity for the rapid diffusion of ions. Consequently, the superior performances of such hierarchical a-MnO$_x$/GS–CNT make this material become a promising candidate for the electrode material of next-generation ECs.

4. Conclusion

A simple, efficient and practical approach to fabricate a novel hierarchical a-MnO$_x$/GS–CNT composite which contains a homoge-neous ultrathin a-MnO$_x$ film with slender nanowires/sheets was proposed through combining a simple solution-assemble process and a cost-effective electrochemical deposition technology. The specific capacitance of a-MnO$_x$ on the desired 3D hierarchical a-MnO$_x$/GS–CNT composite is equal to 1200 F g^{-1} which is much higher than that of pure a-MnO$_x$ (233 F g^{-1}), indicating nearly full utilization of pseudocapacitive manganese species. For the high-power application, a-MnO$_x$/GS–CNT exhibits very high specific energy and specific power (ca. 46.2 Wh kg^{-1} and 33.2 kW kg^{-1}, respectively) under a rapid charge/discharge process (i.e., 5 sec for charging or discharging). The desired 3D hierarchical a-MnO$_x$/GS–CNT with outstanding perfor-mances has been realized by an environment-friendly approach, which is a promising electrode material for the next generation ECs. Moreover, this work conceptually provides a way for tailoring/designing 3D graphene-based materials to many different electrode materials for energy storage and conversion devices.

References

[1] Z. Yang, J. Zhang, M.C.W. Kintner-Meyer, X. Lu, D. Choi, J.P. Lemmon, J. Liu, Chemical Reviews 111 (2011) 3577–3613.

[2] B.E. Conway, Electrochemical Supercapacitors: Scientific Fundamentals and Technological Applications, first ed., Springer, USA, 1999.
[3] P. Simon, Y. Gogotsi, Nature Materials 7 (2008) 845–854.
[4] J.W. Long, D. Belanger, T. Brousse, W. Sugimoto, M.B. Sassin, O. Crosnier, MRS Bulletin 36 (2011) 513–522.
[5] X. Xie, L. Gao, Carbon 45 (2007) 2365–2373.
[6] M. Toupin, T. Brousse, D. Belanger, Chemistry of Materials 16 (2004) 3184–3190.
[7] M. Toupin, T. Brousse, D. Belanger, Chemistry of Materials 14 (2002) 3946–3952.
[8] J.H. Kim, K.H. Lee, L.J. Overzet, G.S. Lee, Nano Letters 11 (2011) 2611–2617.
[9] S.W. Lee, J. Kim, S. Chen, P.T. Hammond, Y. Shao-Horn, ACS Nano 4 (2010) 3889–3896.
[10] S. Chen, J. Zhu, X. Wu, Q. Han, X. Wang, ACS Nano 4 (2010) 2822–2830.
[11] Z. Fan, J. Yan, T. Wei, L. Zhi, G. Ning, T. Li, F. Wei, Advanced Functional Materials 21 (2011) 2366–2375.
[12] J. Zhang, J. Jiang, X. Zhao, The Journal of Physical Chemistry C 115 (2011) 6448–6454.
[13] Q. Cheng, J. Tang, J. Ma, H. Zhang, N. Shinya, L.C. Qin, Carbon 49 (2011) 2917–2925.
[14] J.W. Lee, A.S. Hall, J.D. Kim, T.E. Mallouk, Chemistry of Materials 24 (2012) 1158–1164.
[15] M.D. Stoller, S. Park, Y. Zhu, J. An, R.S. Ruoff, Nano Letters 8 (2008) 3498–3502.
[16] A. Geim, K. Novoselov, Nature Materials 6 (2007) 183–191.
[17] S.Y. Yang, K.H. Chang, H.W. Tien, Y.F. Lee, S.M. Li, Y.S. Wang, J.Y. Wang, C.C.M. Ma, C.C. Hu, Journal of Materials Chemistry 21 (2011) 2374–2380.
[18] D. Li, M.B. Muller, S. Gilje, R.B. Kaner, G.G. Wallace, Nature Nanotechnology 3 (2008) 101–105.
[19] G. Yu, L. Hu, M. Vosgueritchian, H. Wang, X. Xie, J.R. McDonough, X. Cui, Y. Cui, Z. Bao, Nano Letters 11 (2011) 2905–2911.
[20] S. Stankovich, D. Dikin, G. Dommett, K. Kohlhaas, E. Zimney, E. Stach, R. Piner, S. Nguyen, R. Ruoff, Nature 442 (2006) 282–286.
[21] C.C. Hu, K.H. Chang, Journal of the Electrochemical Society 151 (2004) A281.
[22] Y.P. Lin, C.B. Tsai, W.H. Ho, N.L. Wu, Materials Chemistry and Physics 130 (2011) 367–372.
[23] J. Yan, Z. Fan, T. Wei, W. Qian, M. Zhang, F. Wei, Carbon 48 (2010) 3825–3833.
[24] K. Zhang, L.L Zhang, X. Zhao, J. Wu, Chemistry of Materials 22 (2010) 1392–1401.
[25] E. Frackowiak, F. Beguin, Carbon 39 (2001) 937–950.
[26] K.H. Chang, Y.F. Lee, C.C. Hu, C.I. Chang, C.L. Liu, Y.L. Yang, Chemical Communications 46 (2010) 7957–7959.
[27] Y.-H. Chu, C.-C. Hu, K.-H. Chang, Electrochimica Acta 61 (2012) 124–131.
[28] S. Komaba, A. Ogata, T. Tsuchikawa, Electrochemistry Communications 10 (2008) 1435–1437.